RSCPublishing   Faraday Discussions

Theoretical Analysis of the Inverted Region in Photoinduced Proton-Coupled Electron Transfer

Journal:	*Faraday Discussions*
Manuscript ID	FD-ART-12-2018-000240
Article Type:	Paper
Date Submitted by the Author:	14-Dec-2018
Complete List of Authors:	Goldsmith, Zachary; Yale University Soudackov, Alexander; Yale University, Chemistry Hammes-Schiffer, Sharon; Yale University, Department of Chemistry

SCHOLARONE™
Manuscripts

Theoretical Analysis of the Inverted Region in Photoinduced Proton-Coupled Electron Transfer

Zachary K. Goldsmith, Alexander V. Soudackov, and Sharon Hammes-Schiffer*

Department of Chemistry, Yale University, 225 Prospect Street, New Haven, Connecticut 06520

Corresponding e-mail: sharon.hammes-schiffer@yale.edu

Abstract

Photoinduced proton-coupled electron transfer (PCET) plays a key role in a wide range of energy conversion processes, and understanding how to design systems to control the PCET rate constant is a significant challenge. Herein a theoretical formulation of PCET is utilized to identify the conditions under which photoinduced PCET may exhibit inverted region behavior. In the inverted region, the rate constant decreases as the driving force increases even though the reaction becomes more thermodynamically favorable. Photoinduced PCET will exhibit inverted region behavior when the following criteria are satisfied: (1) the overlap integrals corresponding to the ground reactant and the excited product proton vibrational wavefunctions become negligible for a low enough product vibronic state and (2) the reaction free energies associated with the lower excited product proton vibrational wavefunctions contributing significantly to the rate constant are negative with magnitudes greater than the reorganization energy. These criteria are typically not satisfied by harmonic or Morse potentials but are satisfied by more realistic asymmetric double well potentials because the proton vibrational states above the barrier correspond to more delocalized proton vibrational wavefunctions with nodal structures leading to destructive interference effects. Thus, this theoretical analysis predicts that inverted region behavior could be observed for systems with asymmetric double well potentials characteristic of hydrogen-bonded systems and that the hydrogen/deuterium kinetic isotope effect will approach unity and could even become inverse in this region due to the oscillatory nature of the highly excited vibrational wavefunctions. These insights may help guide the design of more effective energy conversion devices.

1. Introduction

Photoinduced proton-coupled electron transfer (PCET) is an essential component of a wide range of energy conversion processes throughout chemistry and biology. Examples of such processes include natural and artificial photosynthesis, as well as photoelectrochemical reduction of carbon dioxide to carbon monoxide or hydrocarbons.[1-8] Given the complexity of these types of processes, which may include many different steps, simple model systems have been designed to enable the investigation of the fundamental underlying physical principles of photoinduced PCET.[9-21] In these model systems, PCET may be initiated by photoexcitation to a metal-to-ligand or ligand-to-metal charge transfer state[9, 11, 14, 15, 17, 18] or to a locally excited state of an aromatic molecular component.[12, 13, 16, 19-21] After this initial photoexcitation, the PCET reaction can occur through a variety of different types of mechanisms involving charge separation and charge recombination.

An interesting question that arises for photoinduced PCET is whether the Marcus inverted region behavior can be observed and, if so, under what conditions it is expected to be observed. In Marcus theory for electron transfer (ET), the rate constant depends exponentially on the free energy barrier,[22, 23] which is expressed in terms of the reaction free energy ΔG^o and the reorganization energy λ as follows:

$$\Delta G^\dagger = \frac{\left(\Delta G^o + \lambda\right)^2}{4\lambda} \ .$$

(2)

Marcus theory predicts an inverted parabola for the dependence of the logarithm of the ET rate constant on the driving force $-\Delta G^o$ (Figure 1). The maximum rate constant is predicted to occur for $-\Delta G^o = \lambda$ because the free energy barrier vanishes and the reaction becomes activationless. In the inverted region, where $-\Delta G^o > \lambda$, the ET rate constant decreases as the driving force increases (i.e., as the reaction becomes more exoergic). The inverted region has been observed

experimentally for electron transfer[24] and is technologically relevant because it has been proposed

to be useful for slowing down charge recombination reactions to avoid wasting energy in energy

conversion processes.[25, 26] However, it can be significantly suppressed for systems with accessible

excited intramolecular vibrational states[27-30] or completely disappear for electrochemical ET due

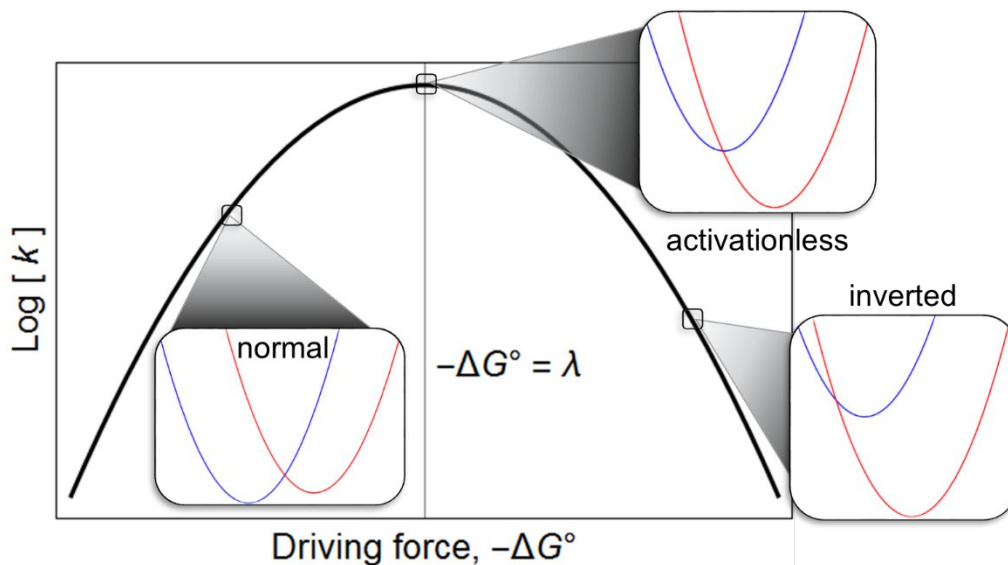to the available continuum of electronic states associated with the electrode.[31-33]

Figure 1. Schematic plot of the logarithm of the rate constant k versus the driving force ΔG^{o} with the free energy barrier given by Eq. (1). The gray vertical line indicates the driving force equal to the reorganization energy λ. Outset are depictions of the normal, activationless, and inverted regions, illustrated by the reactant (blue) and product (red) free energy parabolas as functions of a collective solvent coordinate. In the normal region, the free energy barrier decreases, and the rate constant correspondingly increases, as the driving force increases. The activationless region occurs when $-\Delta G^{o} = \lambda$ and the barrier is zero. In the inverted region, the free energy barrier increases, and the rate constant correspondingly decreases, as the driving force increases.

We have developed a general theory for PCET[34-41] that may be viewed as an extension of

Marcus theory for ET. In this theory, the transferring proton, as well as the active electrons, is

treated quantum mechanically, and the PCET reaction is described in terms of nonadiabatic

transitions between mixed electron-proton vibronic states, correspond to proton vibrational states

for each electronic state (Figure 2). The rate constant is calculated as the Boltzmann-weighted sum

of the rate constants associated with transitions between all pairs of these electron-proton vibronic states, where each term depends exponentially on the corresponding free energy barrier and is proportional to the square of the overlap integral associated with the reactant and product proton vibrational wavefunctions. A previous study from our group[42] suggested that inverted region behavior is unlikely to be observed for PCET reactions because of the availability of excited proton vibrational states associated with the product (Figure 2). As the driving force increases, the free energy barrier for the currently dominant product proton vibrational state increases, but the next excited proton vibrational state becomes nearly activationless and therefore becomes dominant. The accessibility of these excited proton vibrational states causes the rate constant to plateau at higher driving forces, and the inverted region behavior is not observed at experimentally relevant driving forces. However, this previous study was performed using harmonic proton potentials, which are not realistic representations of the bonds between the hydrogen and its donor or acceptor, especially for hydrogen-bonded systems.
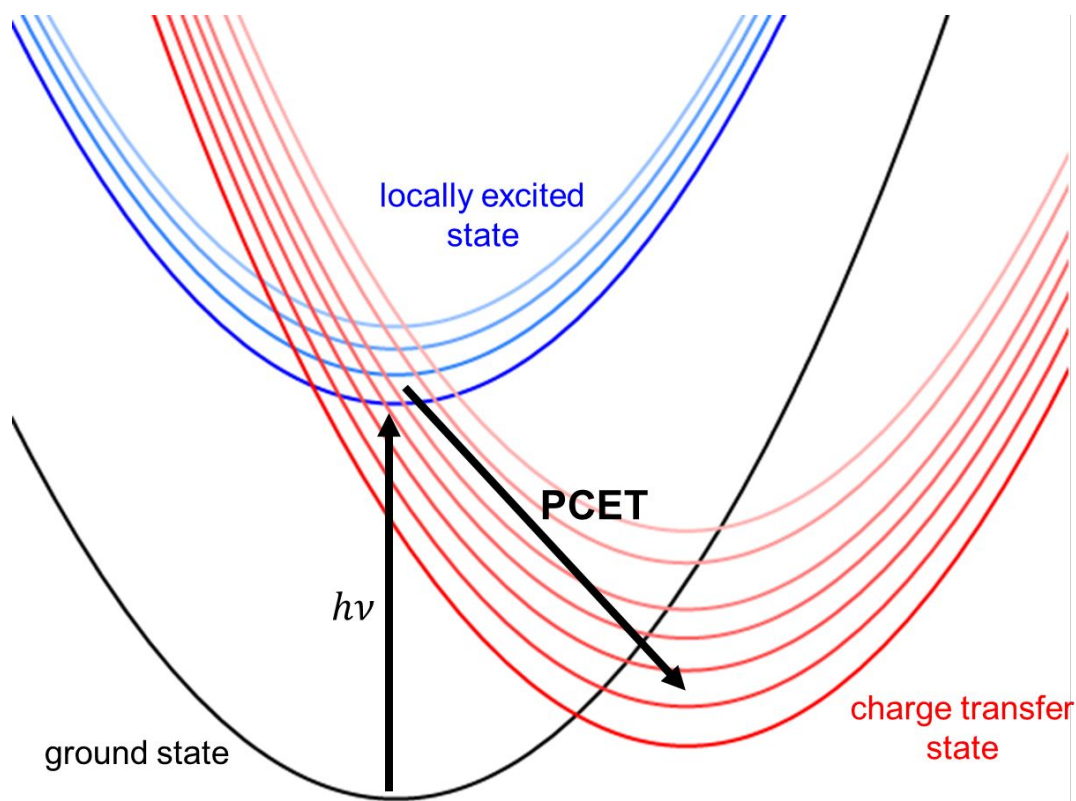
Figure 2. Illustration of a reaction scheme for photoinduced PCET. Photoexcitation from the ground state (black) to a locally excited state (blue) is followed by PCET to a charge transfer state (red), which would subsequently decay to the ground state. The manifolds of stacked parabolas are representative of electron-proton vibronic states, which are essentially proton vibrational states for each electronic state, as functions of a collective solvent coordinate. The calculations presented herein are based on the assumption that vibrational cooling in the locally excited state is faster than PCET, and therefore the PCET reaction occurs from the ground vibronic state (lowest, darkest blue parabola). Moreover, PCET from this locally excited state to the charge transfer state involves transitions that span the normal (higher, lighter red parabolas) and inverted (lower, darker red parabolas) regions that are depicted in Figure 1. This type of PCET process could exhibit inverted region behavior. An alternative situation could occur in which the PCET reaction from the charge transfer state back down to the ground state is more exoergic. In this case, PCET from the ground vibronic state of the charge transfer state (lowest, darkest red parabola) to a manifold of proton vibrational states associated with the ground state (black stacked parabolas not shown here for simplicity) could exhibit inverted region behavior.

Herein we investigate the dependence of the PCET rate constant on the driving force using more realistic proton potentials that are similar to those calculated with density functional theory (DFT) for experimentally studied PCET systems.[43-47] In particular, we perform a comprehensive comparison between the results for a model using Morse potentials and the results for a model

using more realistic asymmetric double well potentials similar to those generated with DFT for real chemical systems. Our analysis illustrates that inverted region behavior is observed under certain conditions that depend on the shape of the proton potential energy curves. We also investigate the hydrogen/deuterium kinetic isotope effects (KIEs) for these model systems and explain why the KIEs become unity, or even slightly less than unity, at large driving forces. These results are also placed in the context of available experimental studies on photoinduced PCET.

2. Nonadiabatic PCET Theory

A general theoretical framework has been developed to describe PCET reactions in solution and proteins.[34-41] In this PCET theory, the transferring proton, as well as the active electrons, are treated quantum mechanically. In the vibronically nonadiabatic regime, the PCET reaction is described in terms of nonadiabatic transitions between reactant and product electron-proton vibronic states. In practice, the proton vibrational states are computed for the reactant and the product diabatic electronic states, and each vibronic state is expressed as the product of one of the diabatic electronic states and an associated proton vibrational state. In this framework, the vibronically nonadiabatic PCET rate constant was derived as a Boltzmann-weighted sum over the rate constants associated with nonadiabatic quantum transitions between all pairs of reactant and product electron-proton vibronic states.

This vibronically nonadiabatic PCET rate constant is expressed as a function of the distance R between the proton donor and acceptor as follows:[35]

$$k(R) = \frac{1}{\hbar}\sqrt{\frac{\pi}{\lambda k_B T}}\sum_{\mu,\nu} P_\mu \left|V_{\mu\nu}(R)\right|^2 \exp\left[-\frac{\Delta G^\dagger_{\mu\nu}}{k_B T}\right]. \tag{3}$$

Here, μ and ν correspond to the reactant and product vibronic states, respectively, P_μ is the Boltzmann population of reactant state μ, $V_{\mu\nu}(R)$ is the vibronic coupling between reactant and

product states μ and v, λ is the total reorganization energy for the reaction, and $\Delta G_{\mu v}^{\dagger}$ is the free

energy barrier associated with the transition between reactant state μ and product state v. The free

energy barrier for reactant/product vibronic state pair (μ,v) is

$$\Delta G_{\mu v}^{\dagger} = \frac{\left(\Delta G_{\mu v}^{o} + \lambda\right)^2}{4\lambda} \ , \tag{4}$$

where $\Delta G_{\mu v}^{o}$ is the reaction free energy associated with vibronic state pair (μ,v). In the

electronically nonadiabatic limit, the vibronic coupling $V_{\mu v}$ is expressed as the product of the

electronic coupling V^{el} and the overlap integral $S_{\mu v}$ between the proton vibrational wavefunctions

associated with reactant/product vibronic state pair (μ,v):

$$V_{\mu v}(R) = V^{\mathrm{el}} S_{\mu v}(R) \ . \tag{5}$$

Note that the electronic coupling is assumed to be independent of the proton donor-acceptor

distance; however, the overlap integral depends strongly on this distance.[37]

The PCET rate constant is thermally averaged over the proton donor-acceptor distance to

obtain the total rate constant, k_{PCET}. This thermal averaging is accomplished by weighting each

rate constant $k(R)$ by the probability distribution $P(R)$ for sampling the proton donor-acceptor

distance R and integrating over this distance:[38, 43, 44]

$$k_{\mathrm{PCET}} = \int_{0}^{\infty} dR \, k(R)P(R) \ . \tag{6}$$

In the present study, the proton donor-acceptor motion is assumed to be harmonic with an

equilibrium proton donor-acceptor distance $\bar{R}$ and an effective force constant k_{eff}. Thus, $P(R)$ is a

normalized Gaussian distribution function with the following form:

$$P(R) = \frac{\exp\left[-k_{\text{eff}}\left(R-\overline{R}\right)^2 / 2k_{\text{B}}T\right]}{\int_{-\infty}^{\infty} \exp\left[-k_{\text{eff}}\left(R-\overline{R}\right)^2 / 2k_{\text{B}}T\right]dR} \quad . \tag{7}$$

3. Model systems for PCET: Morse and asymmetric double well potentials

Two models for the diabatic reactant and product proton potential energy curves were used to probe the conditions for observing the inverted region for PCET. The first model describes the reactant and product proton potential energy curves as Morse potentials, which are nearly harmonic at the equilibrium bond length but also describe bond dissociation. The Morse potentials can be expressed as functions of the proton coordinate r along the proton donor-acceptor axis as follows:

$$U_1(r) = D_e\left[1 - e^{-\beta_1\left(r + \frac{\delta R}{2}\right)}\right]^2 , \tag{8}$$

$$U_2(r) = D_e\left[1 - e^{\beta_2\left(r - \frac{\delta R}{2}\right)}\right]^2 \tag{9}$$

where D_e is the bond dissociation energy and β_1 and β_2 are parameters related to the frequency of the X–H bond for the proton donor and acceptor, respectively. Here δR is the distance between the minima of the two Morse potentials and is related to the proton donor-acceptor distance R by a constant defined as the sum of the two X–H equilibrium bond lengths. For this study, Morse parameters consistent with typical X–H bond frequencies of 3300 cm^{-1} and 3000 cm^{-1} for the proton donor and acceptor, respectively, were chosen. In particular, for the reactant proton potential, D_e = 100 kcal/mol and β_1 = 1.14 Å^{-1}, and for the product proton potential, D_e = 100 kcal/mol and β_2 = 1.04 Å^{-1}. These Morse potentials are depicted in Figure 3A.
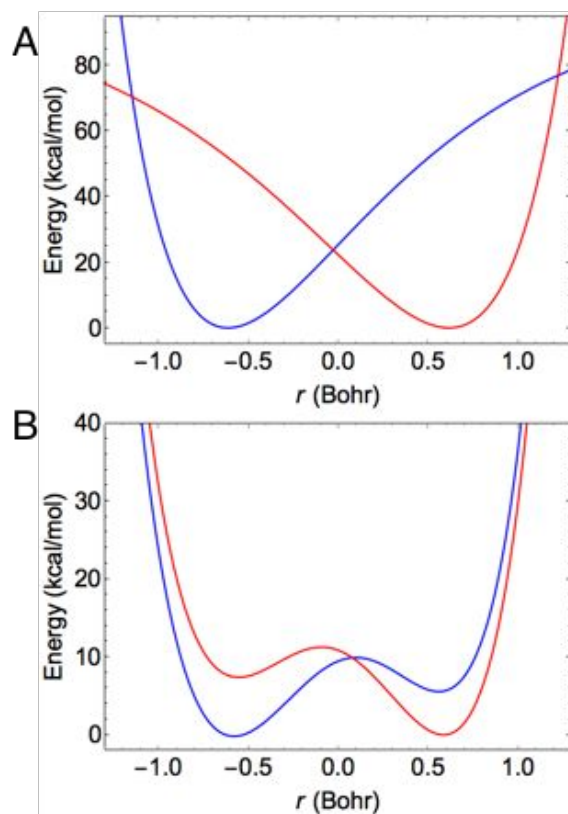
Figure 3. (A) Morse potentials for the model reactant (blue) and product (red) proton potential energy curves associated with the diabatic electronic states. (B) Asymmetric double well potentials for the model reactant (blue) and product (red) proton potential energy curves associated with the diabatic electronic states.

The second model for PCET describes the reactant and product proton potential energy curves as asymmetric double well potentials. Such double well potentials have been commonly observed for PCET systems previously studied by this group using DFT.[43, 45-47] In particular, an asymmetric double well proton potential, or a proton potential with a significant shoulder, is expected to be found when the proton transfer occurs between a donor and acceptor interacting via a relatively strong hydrogen bond.

The asymmetric double well potentials used for this second model system were obtained from the reactant and product Morse potentials used in the first model system. The procedure for obtaining these asymmetric double well potentials at each value of R is as follows:

1. The product Morse potential, $U_2(r)$, is shifted in energy by an asymmetry factor $\pm\Delta$ relative to the minimum of $U_1(r)$. For the reactant, $U_2(r)$ is raised by Δ, and for the product it is lowered by Δ.

2. A 2×2 matrix, given in Eq. (9), is constructed with the shifted Morse potentials as the diagonal elements and a coupling, V^{PT}, as the off-diagonal element:

$$\begin{bmatrix} U_1(r) & V^{PT} \\ V^{PT} & U_2(r) \pm \Delta \end{bmatrix}. \tag{10}$$

3. The matrices described in Eq. (9) are diagonalized, and the lowest eigenvalue for each matrix defines the reactant and product asymmetric double well potentials. For the regions of $|r| > 1.0$ Bohr, switching functions were used to transition smoothly from the lowest eigenvalue to the corresponding higher-energy diabatic potentials to circumvent unphysical avoided crossing points in these regions.

For this study, the energetic shift Δ was chosen to be 10 kcal/mol, and the coupling V^{PT} was chosen to be 30 kcal/mol. The reactant and product asymmetric double well potentials are depicted in Figure 3B.

For each proton potential, the proton or deuteron vibrational wavefunctions and their energy levels were obtained by solving the one-dimensional Schrödinger equation analytically[48] for the Morse potentials or numerically[49] for the asymmetric double well potentials. The proton vibrational wavefunctions for the model systems described above are depicted in Figure 4. This figure illustrates that the proton vibrational wavefunctions for the reactant and product Morse potentials are much more localized than those for the asymmetric double well potentials. This characteristic difference will have consequences in terms of the overlap integrals, $S_{\mu\nu}$, in the rate constant calculations. Furthermore, the proton vibrational states above the barrier for the asymmetric double well potentials exhibit significantly smaller energy level splittings than those

for the Morse potentials, influencing the reaction free energies in the rate constant calculations.

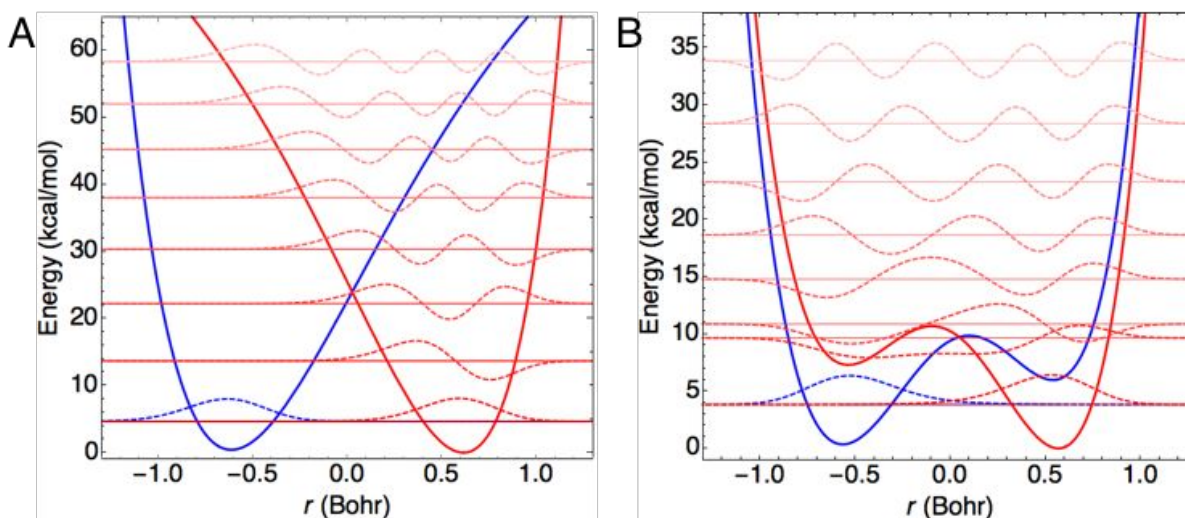These issues will be discussed further below.

Figure 4. Model reactant (blue, solid) and product (red, solid) proton potentials and the associated proton vibrational energy levels (horizontal lines) and wavefunctions (dashed curves) for the (A) Morse and (B) asymmetric double well potentials. Only the ground proton vibrational state for the reactant is shown along with a series of excited product proton vibrational states ($v = 0-7$). Note that the smaller energy scale in B indicates a much denser manifold of proton vibrational states (i.e., smaller splittings between the energy levels) for the asymmetric double well potentials than for the Morse potentials.

4. Relationship between driving force and PCET rate constant for model systems

The plausibility of observing the Marcus inverted region for PCET was investigated by calculating k_{PCET} over a range of driving forces ($-\Delta G$) from zero to values significantly larger in magnitude than λ for both model systems. The qualitative behavior is not altered by the specific values of the parameters entering the rate constant expression, and we chose values that are similar to those calculated for PCET systems previously studied in our group. The force constant associated with the harmonic proton donor-acceptor motion was chosen to be $k_{eff} = 0.051$ au, which is comparable to previously computed values for intramolecular, hydrogen-bonded PCET systems.[45] The reorganization energy was chosen to be $\lambda = 25$ kcal/mol, which is consistent with many calculated and experimental values for outer-sphere ET and PCET.[50] Lastly, the electronic

coupling was chosen to be $V^{el} = 1$ kcal/mol. The electronic coupling is simply a constant scaling factor in the expression for k_{PCET} and does not impact the relationship between the rate constant and the driving force or the KIE. In all calculations, the number of electron-proton vibronic states included was fully converged, which required a significant number of product states (i.e., up to 16 for the Morse potentials and 28 for the asymmetric double well potentials) for the highly exoergic reactions. The relationships between the driving force and k_{PCET}, as well as the KIE, for both types of model potentials are shown in Figure 5.
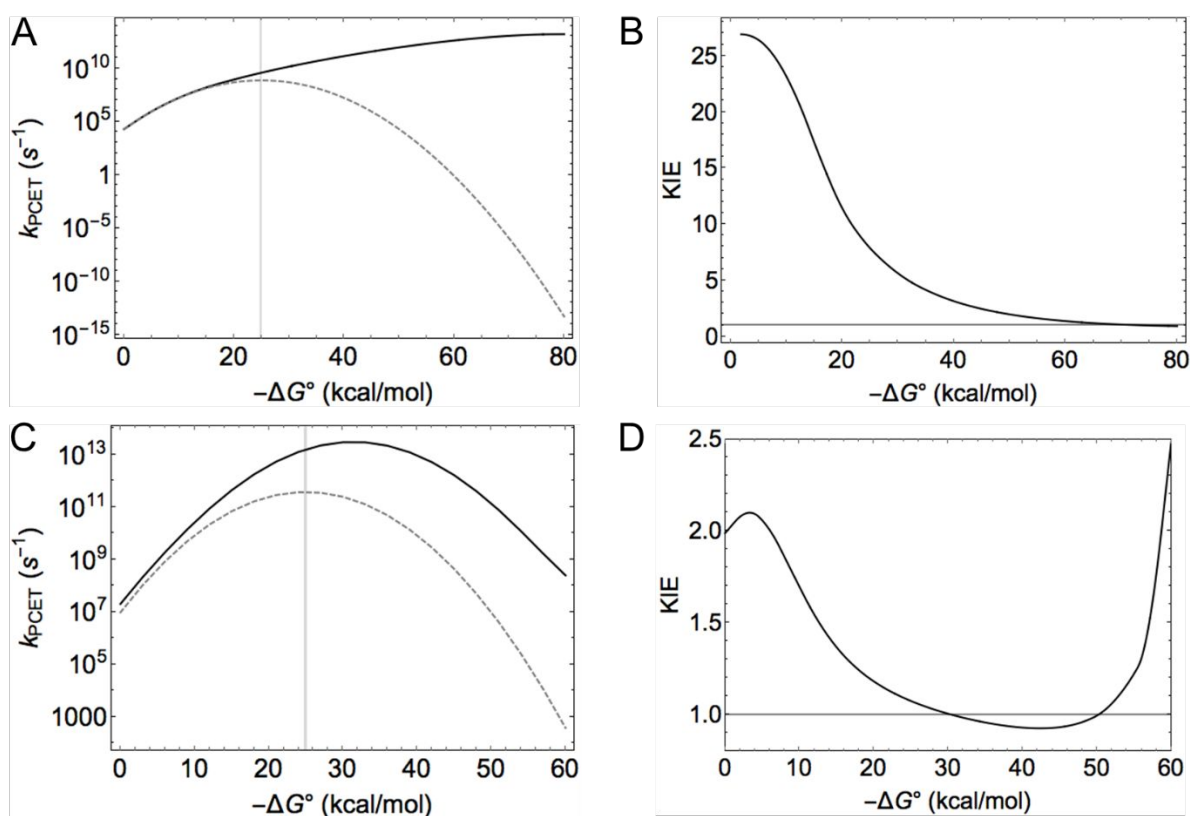

Figure 5. Driving force dependence of the rate constant k_{PCET} and the KIE for Morse (A, B) and asymmetric double well (C, D) proton potentials. In A and C, the dashed gray curves depict the rate constant calculated with only the transition from the ground reactant to the ground product vibronic state (i.e., the (0,0) vibronic state pair), whereas the solid black curves depict the rate constant including contributions from the excited proton vibrational states.. The solid gray vertical line in A and C corresponds to $\lambda = 25$ kcal/mol. In B and D, the horizontal gray lines at KIE = 1 represent the situation in which the rate constants of PCET with hydrogen and deuterium are equal.

As shown previously for harmonic potentials,[42] the inverted region for PCET is not observed for the model system using Morse potentials (Figure 5A). Neglecting the excited proton vibrational state contributions to the rate constant (i.e., including only the (0,0) vibronic state pair) yields a clear attenuation in the total rate constant at driving forces greater than λ (Figure 5A, dashed gray line). In contrast, the results including the contributions from the excited proton vibrational states exhibit no apparent decrease in the rate constant up to $-\Delta G^o = 80$ kcal/mol. In other words, the rate constant k_{PCET} approaches a plateau for the larger driving forces. We found that the computed k_{PCET} appears to start decreasing at ca. $-\Delta G^o = 90-100$ kcal/mol, but these rate constants may not be fully converged with respect to bound product proton vibrational states given the dissociation energy of 100 kcal/mol for the product Morse potential. Figure 5 only shows the data for which the results are fully converged.

The KIEs calculated for the model with Morse potentials demonstrate a strong driving force dependence (Figure 5B). At lower driving forces, corresponding to a virtually isoergic reaction, the KIE was computed to be nearly 30. As the driving force for the PCET reaction increases, this calculated KIE decreases nearly monotonically to unity. As will be demonstrated below, the highly delocalized nature of the proton vibrational wavefunctions predominantly contributing to the rate constant at higher driving forces attenuates the difference in overlap integrals between hydrogen and deuterium. Conversely, at lower driving forces, the ground-to-ground state transition is dominant, as illustrated by the overlap between the solid black and dashed gray lines for lower driving forces in Figure 5A. The ground state proton vibrational wavefunctions are much more localized (Figure 4A), and therefore the associated overlap integrals are extremely sensitive to the change in the mass of the transferring nucleus.

In contrast to the results with Morse potentials, as well as the previous results with harmonic potentials,[42] the inverted region can be clearly observed for the model using asymmetric double well proton potentials (Figure 5C). Shortly after $-\Delta G^o$ exceeds λ, the value of the rate constant begins to decrease. The contributions from the excited proton vibrational states lead to asymmetry and shifting of the maximum of the inverted parabola describing the driving force dependence of the rate constant, as observed previously for ET reactions coupled to a vibrational quantum mode.[27, 28]

The KIEs for the model with asymmetric double well potentials (Figure 5D) are around 2 at low driving forces. These KIEs are significantly smaller than those obtained from the model with Morse potentials at low driving forces (Figure 5B). As the driving force increases, the KIE decreases predominantly monotonically to unity and even slightly below unity until it starts to increase very rapidly for the most exoergic driving forces studied. The unexpected observation of inverse KIEs (i.e., KIEs smaller than unity), which have also been observed experimentally,[15] and the increase in the KIE at higher driving forces[28] are due to a complex balance among the various contributions to the rate constants for hydrogen and deuterium. The inverse KIE most likely arises from greater vibrational wavefunction overlap integrals for deuterium than for hydrogen for the vibronic state pairs with dominant contributions to the corresponding rate constants. These issues will be analyzed in detail in the next section.

5. Analysis of vibronic state contributions to the rate constant

To further elucidate why the inverted region is or is not observed for these model systems, the contributions of individual reactant/product vibronic state pairs (μ,v) to the total rate constant at significantly exoergic driving forces were analyzed. Thermal averaging over the proton donor-

15

acceptor distance often avails larger proton vibrational wavefunction overlaps at smaller values of R, leading to a dominant proton donor-acceptor distances (i.e., the distance R corresponding to the maximum of the integrand in Eq. (5)) that are shorter than the equilibrium proton donor-acceptor distance.[45] For both types of model potentials studied herein, however, the dominant proton donor-acceptor distance was determined to be very close to the equilibrium distance. This dominance of the equilibrium proton donor-acceptor distance is a consequence of significant contributions from highly delocalized wavefunctions to the total rate constant, thereby avoiding the necessity of sampling the smaller, less energetically favorable proton donor-acceptor distances. Thus, we analyzed the contributions from the individual reactant/product vibronic state pairs at the equilibrium proton donor-acceptor distance with $\delta R = 1.20$ Bohr.

We analyzed these contributions at a driving force of 60 kcal/mol. At this driving force, Figures 5A and 5C indicate that the asymmetric double well model system is exhibiting inverted region behavior (i.e., the rate constant is decreasing as the driving force increases), whereas the Morse system is not exhibiting this behavior (i.e., the rate constant is slightly increasing as the driving force increases). The relative contributions of the individual reactant/product vibronic state pairs to the rate constant are determined by a balance between the square of the overlap integral, $S^2_{\mu\nu}$, and the exponential of the free energy barrier, $\Delta G^\dagger_{\mu\nu}$. These and other associated quantities, as well as the percentage contribution to the total rate constant, are given in Tables 1 and 2 for the relevant vibronic state pairs (μ,ν).

Table 1. Main contributions to the rate constant at $\Delta G^{\mathrm{o}} = -60$ kcal/mol for Morse potentials with $\delta R = 1.20$ Bohr.[a]

(μ,ν)	$\Delta G^{\mathrm{o}}_{\mu\nu}$	$\Delta G^{\dagger}_{\mu\nu}$	$\exp\left[-\Delta G^{\dagger}_{\mu\nu}\Big/k_{\mathrm{B}}T\right]$	$S^2_{\mu\nu}$	% Contrib.
(0,0)	−60.00	12.25	1.05 x 10⁻⁹	7.27 x 10⁻⁷	0.00
(0,1)	−51.00	6.76	1.11 x 10⁻⁵	2.37 x 10⁻⁵	0.00
(0,2)	−42.44	3.04	5.90 x 10⁻³	3.69 x 10⁻⁴	0.00
(0,3)	−34.33	0.87	2.30 x 10⁻¹	3.51 x 10⁻³	0.86
(0,4)	−26.67	0.03	9.54 x 10⁻¹	2.18 x 10⁻²	22.26
(0,5)	−19.45	0.31	5.94 x 10⁻¹	8.91 x 10⁻²	56.71
(0,6)	−12.68	1.52	7.71 x 10⁻²	2.31 x 10⁻¹	19.09
(0,7)	−6.35	3.48	2.83 x 10⁻³	3.49 x 10⁻¹	1.06

[a]Free energies in kcal/mol.

Table 2. Main contributions to the rate constant at $\Delta G^{\mathrm{o}} = -60$ kcal/mol for asymmetric double well potentials with $\delta R = 1.20$ Bohr.[a]

(μ,ν)	$\Delta G^{\mathrm{o}}_{\mu\nu}$	$\Delta G^{\dagger}_{\mu\nu}$	$\exp\left[-\Delta G^{\dagger}_{\mu\nu}\Big/k_{\mathrm{B}}T\right]$	$S^2_{\mu\nu}$	% Contrib.
(0,0)	-60.00	12.25	1.05 x 10⁻⁹	1.93 x 10⁻³	0.00
(0,1)	-54.18	8.52	5.73 x 10⁻⁷	5.90 x 10⁻¹	4.14
(0,2)	-52.96	7.82	1.85 x 10⁻⁶	3.72 x 10⁻¹	8.44
(0,3)	-49.05	5.78	5.78 x 10⁻⁵	3.40 x 10⁻²	24.00
(0,4)	-45.18	4.07	1.03 x 10⁻³	1.53 x 10⁻³	19.33
(0,5)	-40.56	2.42	1.68 x 10⁻²	1.08 x 10⁻⁵	2.22
(0,6)	-35.47	1.10	1.57 x 10⁻¹	1.82 x 10⁻⁵	34.99
(0,7)	-29.95	0.25	6.61 x 10⁻¹	7.96 x 10⁻⁷	6.44
(0,8)	-24.05	0.01	9.85 x 10⁻¹	2.19 x 10⁻⁸	0.26

[a]Free energies in kcal/mol.

Table 1 demonstrates that the dominant contribution to the rate constant for the model with Morse potentials is from vibronic state pair (0,5), which constitutes ~57% of the total rate constant. The pairs (0,4) and (0,6) also each constitute ~20% of the total rate. Note that the value of $\Delta G^{\dagger}_{\mu\nu}$ is quite small for all three of these vibronic state pairs, and pair (0,4) is virtually activationless, with a free energy barrier of only 0.03 kcal/mol. The monotonic increase in the overlap integrals

17

as the product proton vibrational state index v increases results in the (0,5) pair contributing more than the (0,4) pair to the total rate constant. The dominant (0,5) pair is associated with a reaction free energy of $\Delta G^o_{\mu v} = -19.45$ kcal/mol, which is smaller in magnitude than λ. Thus, although the driving force, $-\Delta G^o = -\Delta G^o_{00}$ (i.e., the reaction free energy for the (0,0) vibronic state pair), is much larger than λ, the reaction free energy for the dominant reactant/product vibronic state pair is in the normal region. Therefore, we observe that k_{PCET} is still increasing for the Morse potential model system at $\Delta G^o = -60$ kcal/mol. This trend continues as the driving force increases, with greater contributions from even higher excited product proton vibrational states because the overlap integrals continue to increase.

Table 2 indicates that more reactant/product vibronic state pairs contribute significantly to the total rate constant at this driving force for the model with asymmetric double well potentials. The largest contribution to the total rate constant for this model is from the (0,6) pair, which constitutes ~35% of the total rate constant. This pair is followed by pairs (0,3) and (0,4), which constitute ~24% and ~19%, respectively, of the total rate constant. Smaller contributions are associated with the (0,1), (0,2), (0,5), and (0,7) pairs as well. For each of these pairs, however, the value of $\Delta G^o_{\mu v}$ is greater in magnitude than λ. In other words, despite the participation of excited product proton vibrational states, those vibrational states that contribute significantly possess the key characteristic of the inverted region. Thus, at $\Delta G^o = -60$ kcal/mol, the asymmetric double well model system exhibits inverted region behavior.

The vibronic state pair in the asymmetric double well model system corresponding to an activationless transition is the (0,8) pair, which is associated with a free energy barrier of only 0.01 kcal/mol. This pair contributes negligibly to the rate constant, however, because the square of the proton vibrational wavefunction overlap integral, $S^2_{\mu v}$, is prohibitively small with a value of ~10-

[8]. All of the vibronic state pairs that contribute considerably to the total rate constant have values of $S_{\mu\nu}^2$ at least three orders of magnitude greater than that of the activationless (0,8) pair. Specifically, the dominant pairs, (0,6), (0,3), and (0,4), have values of $S_{\mu\nu}^2$ in the range of $10^{-2} - 10^{-5}$, rather than 10^{-8}. For the model system with asymmetric double well potentials, the highly excited product proton vibrational states (i.e., those corresponding to $v > 7$) become inaccessible because of the small overlap integrals (Figure 6), which arise from phase cancellation between the ground reactant state proton vibrational wavefunction and the highly oscillatory excited state product proton vibrational wavefunctions. Thus, this model system exhibits inverted region behavior with the maximum of the inverted parabola shifted to a value slightly greater than λ due to contributions from excited proton vibrational states.

The overlap integrals of the ground reactant proton vibrational state with various product proton vibrational states are depicted in Figure 6 for both model systems and for both hydrogen and deuterium. For the Morse potential model system (Figure 6A), the overlap integrals S_{0v} steadily grow as v increases from zero to seven and subsequently decrease non-monotonically to small but not negligible values. This same trend is observed for deuterium in the Morse potential model (Figure 6B), although it is spread over a larger range of product vibrational quantum numbers v with the maximum shifted to a larger value of v. Qualitatively different behavior of the overlap integral S_{0v} is observed for the asymmetric double well model (Figures 6C and 6D). For this model, the proton vibrational wavefunction overlap integrals increase very rapidly with v, peaking at $v = 1$ for hydrogen and $v = 2$ for deuterium. As v further increases, S_{0v} decreases rapidly, becoming very small much more quickly than for the Morse potential model. Thus, the overlap integral becomes negligible for the asymmetric double well potential model at a quantum number v for which the overlap is significant for the Morse potential model. As discussed further below, this
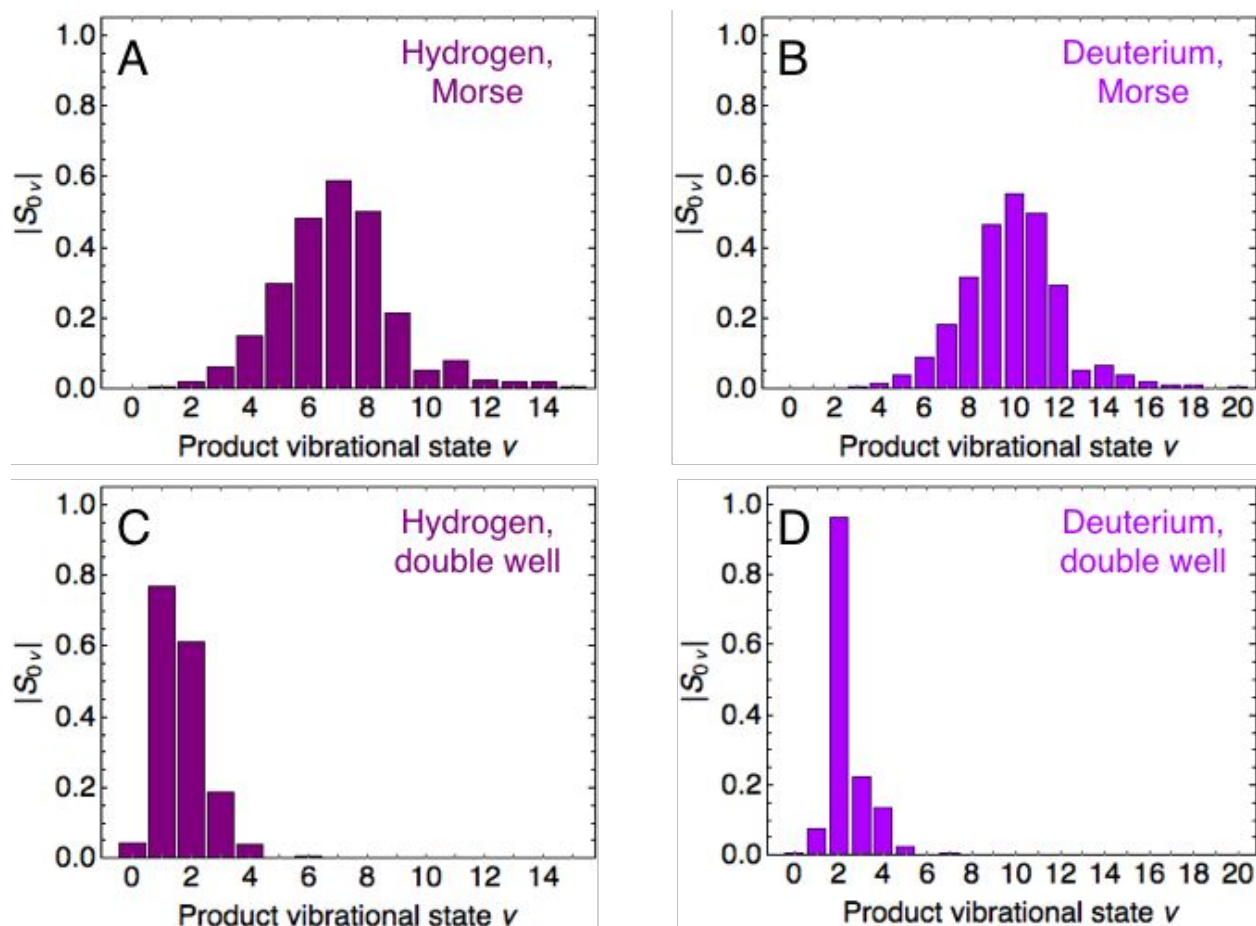
19

Figure 6. Absolute overlap integrals between the ground reactant proton vibrational wavefunction and the product proton vibrational wavefunctions v at $\delta R = 1.20$ Bohr for the Morse potentials (A, B) and asymmetric double well potentials (C, D) for hydrogen (A, C) and deuterium (B, D) transfer.

difference is the main basis for the observation of the inverted region for the asymmetric double well potential model but not for the Morse potential model. Furthermore, the smaller overlap integrals for the lower product proton vibrational states in the Morse potential model provide anexplanation for the much greater KIEs for the Morse potential model systems at lower driving forces, where these lower proton vibrational states dominate. In general, smaller overlap integrals for the dominant vibronic state pairs lead to larger KIEs.[39, 41]

In addition, the proton vibrational states in the asymmetric double well potentials are much more energetically dense (i.e., the energy level splittings are smaller) than are those in the Morse

potentials (Figure 4). The reason for the smaller energy level splittings in the asymmetric double well potentials is that the excited proton vibrational states are above the barrier and thus correspond to a softer potential than is associated with the Morse potentials. As a result, the reaction free energy associated with a given $(0,v)$ pair is more negative for the asymmetric double well potential model than for the Morse potential model, leading to inverted region behavior for the former and not for the latter.

The difference in the accessibility of highly excited product proton vibrational states for the asymmetric double well potentials compared to the Morse potentials explains why the inverted region behavior is observed for the former but not for the latter. Specifically, the overlap integrals associated with the relevant excited product proton vibrational states increase for the Morse potentials but become virtually zero for the asymmetric double well potentials. As a result, a progressively more excited product proton vibrational state becomes dominant as the driving force increases for the Morse potentials, preventing inverted region behavior. Because these excited product proton vibrational states are inaccessible for the asymmetric double well potentials due to the vanishing overlap integrals, the lower excited proton vibrational states continue to dominate as the driving force increases for the asymmetric double well potentials, leading to inverted region behavior.

6. Conclusions

The analysis presented herein indicates that inverted region behavior can be observed for photoinduced PCET reactions under certain conditions. The first condition is that the overlap integrals corresponding to the ground reactant and the product proton vibrational states decrease rapidly for higher excited product proton vibrational states. As a result, the highly excited proton

vibrational states do not contribute to the rate constant, and the mid-level excited proton vibrational states remain dominant. The second condition is that the energy splittings between these mid-level excited proton vibrational states are small enough to ensure that the associated reaction free energies of the dominant states are negative with magnitudes greater than the reorganization energy. These conditions are typically not satisfied by harmonic and Morse potentials, and therefore inverted region behavior is not expected to be observed for these types of potentials. In contrast, these conditions were found to be satisfied by the more realistic asymmetric double well potentials studied herein because the mid-level excited proton vibrational states are more delocalized with smaller energy level splittings. Moreover, these excited proton vibrational wavefunctions are highly oscillatory, leading to destructive interference effects in the overlap with the ground reactant proton vibrational wavefunction. Thus, inverted region behavior is predicted to be observed for systems with these types of proton potentials, which are expected to be found in relatively strongly hydrogen-bonded systems. In addition, the KIE is expected to approach unity and could even become inverse as the driving force increases because the oscillatory nature of the highly excited vibrational wavefunctions produces overlap integrals that do not distinguish significantly between hydrogen and deuterium.

These calculations provide guidance in designing systems that could exhibit inverted region behavior. An underlying assumption of the PCET rate constant used herein is that the reactant is equilibrated in terms of the proton vibrational state populations and the solvent configuration. Thus, vibrational cooling and solvent relaxation are assumed to be faster than the lifetime of the reactant state. Examples of the types of experimentally attainable processes that could potentially exhibit inverted region behavior are photoexcitation to a locally excited state that undergoes exoergic PCET to a charge transfer state, or alternatively photoexcitation to a locally

excited state, which relaxes to a charge transfer state that then undergoes exoergic PCET back down to the ground state. A wide range of other experimental scenarios are also possible. Observation of inverted region behavior is more likely for proton transfer across a hydrogen-bonded interface corresponding to asymmetric double well proton potential energy curves and also requires tuning of the reorganization energy and the optoelectronic properties of the photochemical system. These design principles may be helpful in the development of more effective and efficient energy conversion devices.

Acknowledgements

References

1. C. Tommos and G. T. Babcock, *Biochim. Biophys. Acta Bioenerg.*, 2000, **1458**, 199-219.
2. T. J. Meyer, M. H. V. Huynh and H. H. Thorp, *Angew. Chem. Int. Ed.*, 2007, **46**, 5284-5304.
3. L. Hammarström and S. Styring, *Philos. Trans. Royal Soc. B*, 2008, **363**, 1283-1291.
4. A. J. Morris, G. J. Meyer and E. Fujita, *Acc. Chem. Res.*, 2009, **42**, 1983-1994.
5. S. C. Roy, O. K. Varghese, M. Paulose and C. A. Grimes, *ACS Nano.*, 2010, **4**, 1259-1278.
6. L. Hammarström and S. Styring, *Energy Env. Sci.*, 2011, **4**, 2379-2388.
7. D. R. Weinberg, C. J. Gagliardi, J. F. Hull, C. F. Murphy, C. A. Kent, B. C. Westlake, A. Paul, D. H. Ess, D. G. McCafferty and T. J. Meyer, *Chem. Rev.*, 2012, **112**, 4016-4093.
8. L. Hammarström, *Acc. Chem. Res.*, 2015, **48**, 840-850.
9. C. Turró, J. M. Zaleski, Y. M. Karabatsos and D. G. Nocera, *J. Am. Chem. Soc.*, 1996, **118**, 6060-6067.
10. J. P. Kirby, J. A. Roberts and D. G. Nocera, *J. Am. Chem. Soc.*, 1997, **119**, 9230-9236.
11. C. J. Gagliardi, B. C. Westlake, C. A. Kent, J. J. Paul, J. M. Papanikolas and T. J. Meyer, *Coord. Chem. Rev.*, 2010, **254**, 2459-2471.
12. J. N. Schrauben, M. Cattaneo, T. C. Day, A. L. Tenderholt and J. M. Mayer, *J. Am. Chem. Soc.*, 2012, **134**, 16635-16645.
13. T. T. Eisenhart and J. L. Dempsey, *J. Am. Chem. Soc.*, 2014, **136**, 12221-12224.
14. O. S. Wenger, *Coord. Chem. Rev.*, 2015, **282-283**, 150-158.
15. G. F. Manbeck, E. Fujita and J. J. Concepcion, *J. Am. Chem. Soc.*, 2016, **138**, 11536-11549.
16. E. W. Driscoll, J. R. Hunt and J. M. Dawlaty, *J. Phys. Chem. Lett.*, 2016, **7**, 2093-2099.
17. J. C. Lennox and J. L. Dempsey, *J. Phys. Chem. B*, 2017, **121**, 10530-10542.
18. J. C. Lennox, D. A. Kurtz, T. Huang and J. L. Dempsey, *ACS Energy Lett.*, 2017, **2**, 1246-1256.
19. S. D. Glover, G. A. Parada, T. F. Markle, S. Ott and L. Hammarström, *J. Am. Chem. Soc.*, 2017, **139**, 2090-2101.
20. M. A. Bowring, L. R. Bradshaw, G. A. Parada, T. P. Pollock, R. J. Fernández-Terán, S. S. Kolmar, B. Q. Mercado, C. W. Schlenker, D. R. Gamelin and J. M. Mayer, *J. Am. Chem. Soc.*, 2018, **140**, 7449-7452.
21. J. R. Hunt and J. M. Dawlaty, *J. Phys. Chem. A*, 2018, **122**, 7931-7940.
22. R. A. Marcus, *J. Chem. Phys.*, 1965, **43**, 2654-2657.
23. R. A. Marcus and N. Sutin, *Biochim. Biophys. Acta Bioenerg.*, 1985, **811**, 265-322.
24. G. L. Closs and J. R. Miller, *Science*, 1988, **240**, 440.
25. H. Imahori, K. Tamaki, D. M. Guldi, C. Luo, M. Fujitsuka, O. Ito, Y. Sakata and S. Fukuzumi, *J. Am. Chem. Soc.*, 2001, **123**, 2607-2617.
26. D. I. Schuster, P. Cheng, P. D. Jarowski, D. M. Guldi, C. Luo, L. Echegoyen, S. Pyo, A. R. Holzwarth, S. E. Braslavsky, R. M. Williams and G. Klihm, *J. Am. Chem. Soc.*, 2004, **126**, 7257-7270.
27. J. Ulstrup and J. Jortner, *J. Chem. Phys.*, 1975, **63**, 4358-4368.
28. M. Bixon and J. Jortner, *Farad. Discuss.*, 1982, **74**, 17-29.
29. M. Bixon and J. Jortner, *J. Phys. Chem.*, 1991, **95**, 1941-1944.
30. M. D. Newton, *Coord. Chem. Rev.*, 2003, **238-239**, 167-185.

31.	R. A. Marcus, *Annu. Rev. Phys. Chem.*, 1964, **15**, 155-196.
32.	W. Schmickler and E. Santos, *Interfacial Electrochemistry*, Springer, 2 edn., 1996.
33.	A. Nitzan, *J. Phys. Chem. A*, 2001, **105**, 2677-2679.
34.	A. Soudackov and S. Hammes-Schiffer, *J. Chem. Phys.*, 1999, **111**, 4672-4687.
35.	A. Soudackov and S. Hammes-Schiffer, *J. Chem. Phys.*, 2000, **113**, 2385-2396.
36.	S. Hammes-Schiffer, *Acc. Chem. Res.*, 2001, **34**, 273-281.
37.	A. Soudackov, E. Hatcher and S. Hammes-Schiffer, *The Journal of Chemical Physics*, 2005, **122**, 014505.
38.	S. Hammes-Schiffer, E. Hatcher, H. Ishikita, J. H. Skone and A. V. Soudackov, *Coord. Chem. Rev.*, 2008, **252**, 384-394.
39.	S. Hammes-Schiffer and A. V. Soudackov, *J. Phys. Chem. B*, 2008, **112**, 14108-14123.
40.	S. Hammes-Schiffer and A. A. Stuchebrukhov, *Chem. Rev.*, 2010, **110**, 6939-6960.
41.	S. Hammes-Schiffer, *J. Am. Chem. Soc.*, 2015, **137**, 8860-8871.
42.	S. J. Edwards, A. V. Soudackov and S. Hammes-Schiffer, *J. Phys. Chem. B*, 2009, **113**, 14545-14548.
43.	B. Auer, L. E. Fernandez and S. Hammes-Schiffer, *J. Am. Chem. Soc.*, 2011, **133**, 8282-8292.
44.	S. Horvath, L. E. Fernandez, A. V. Soudackov and S. Hammes-Schiffer, *Proc. Nat. Acad. Sci. USA*, 2012, **109**, 15663.
45.	M. T. Huynh, S. J. Mora, M. Villalba, M. E. Tejeda-Ferrari, P. A. Liddell, B. R. Cherry, A.-L. Teillout, C. W. Machan, C. P. Kubiak, D. Gust, T. A. Moore, S. Hammes-Schiffer and A. L. Moore, *ACS Cent. Sci.*, 2017, **3**, 372-380.
46.	P. Li, A. V. Soudackov and S. Hammes-Schiffer, *J. Am. Chem. Soc.*, 2018, **140**, 3068-3076.
47.	E. R. Sayfutyarova, Z. K. Goldsmith and S. Hammes-Schiffer, *J. Am. Chem. Soc.*, 2018, **140**, 15641-15645.
48.	H. Taseli, *J. Phys. A Math. Gen.*, 1998, **31**, 779.
49.	S. P. Webb and S. Hammes-Schiffer, *J. Chem. Phys.*, 2000, **113**, 5214-5227.
50.	S. Ghosh, S. Horvath, A. V. Soudackov and S. Hammes-Schiffer, *J. Chem. Theory Comput.*, 2014, **10**, 2091-2102.